

Journal of Astronomical Telescopes, Instruments, and Systems

AstronomicalTelescopes.SPIEDigitalLibrary.org

$\lambda = 2.4$ to $5 \mu\text{m}$ spectroscopy with the James Webb Space Telescope NIRCam instrument

Thomas P. Greene
Douglas M. Kelly
John Stansberry
Jarron Leisenring
Eiichi Egami
Everett Schlawin
Laurie Chu
Klaus W. Hodapp
Marcia Rieke

SPIE.

Thomas P. Greene, Douglas M. Kelly, John Stansberry, Jarron Leisenring, Eiichi Egami, Everett Schlawin, Laurie Chu, Klaus W. Hodapp, Marcia Rieke, “ $\lambda = 2.4$ to $5 \mu\text{m}$ spectroscopy with the James Webb Space Telescope NIRCam instrument,” *J. Astron. Telesc. Instrum. Syst.* **3**(3), 035001 (2017), doi: 10.1117/1.JATIS.3.3.035001.

$\lambda = 2.4$ to $5 \mu\text{m}$ spectroscopy with the James Webb Space Telescope NIRC*am* instrument

Thomas P. Greene,^{a,*} Douglas M. Kelly,^b John Stansberry,^c Jarron Leisenring,^b Eiichi Egami,^b Everett Schlawin,^b Laurie Chu,^d Klaus W. Hodapp,^d and Marcia Rieke^b

^aNASA Ames Research Center, Moffett Field, California, United States

^bUniversity of Arizona, Steward Observatory, Tucson, Arizona, United States

^cSpace Telescope Science Institute, Baltimore, Maryland, United States

^dUniversity of Hawaii, Institute for Astronomy, Hilo, Hawaii, United States

Abstract. The James Webb Space Telescope near-infrared camera (JWST NIRC*am*) has two 2.2×2.2 fields of view that can be observed with either imaging or spectroscopic modes. Either of two $R \sim 1500$ gratings with orthogonal dispersion directions can be used for slitless spectroscopy over $\lambda = 2.4$ to $5.0 \mu\text{m}$ in each module, and shorter wavelength observations of the same fields can be obtained simultaneously. We describe the design drivers and parameters of the gratings and present the latest predicted spectroscopic sensitivities, saturation limits, resolving powers, and wavelength coverage values. Simultaneous short wavelength (0.6 to $2.3 \mu\text{m}$) imaging observations of the 2.4 to $5.0 \mu\text{m}$ spectroscopic field can be performed in one of several different filter bands, either in focus or defocused via weak lenses internal to the NIRC*am*. The gratings are available for single-object time-series spectroscopy and wide-field multiobject slitless spectroscopy modes in the first cycle of JWST observations. We present and discuss operational considerations including subarray sizes and data volume limits. Potential scientific uses of the gratings are illustrated with simulated observations of deep extragalactic fields, dark clouds, and transiting exoplanets. Information needed to plan observations using these spectroscopic modes is also provided. © The Authors. Published by SPIE under a Creative Commons Attribution 3.0 Unported License. Distribution or reproduction of this work in whole or in part requires full attribution of the original publication, including its DOI. [DOI: [10.1117/1.JATIS.3.3.035001](https://doi.org/10.1117/1.JATIS.3.3.035001)]

Keywords: infrared spectroscopy; satellites; space optics; gratings; cameras.

Paper 17010P received Mar. 28, 2017; accepted for publication Jun. 21, 2017; published online Jul. 17, 2017.

1 Introduction

The near-infrared camera (NIRC*am*) of the James Webb Space Telescope (JWST) has flexible modes that provide wide-field imaging through narrow-, medium-, or wide-band filters, coronagraphic imaging, and slitless spectroscopy.^{1–5} Long wavelength (LW; $\lambda = 2.4$ to $5.0 \mu\text{m}$) Si gratings⁶ and $\lambda = 1$ to $2 \mu\text{m}$ dispersed Hartmann sensors (DHSs) were developed for the purposes of wavefront sensing and telescope primary segment phasing with NIRC*am*.⁷ The DHSs provide $R \equiv \lambda/\delta\lambda \approx 300$ spectra of bright point sources.⁸ The LW gratings have been approved and are being supported for scientific use in cycle 1 and later, and the DHSs are being considered for scientific use after cycle 1.

The NIRC*am* instrument is composed of two nearly identical optical modules (A and B), each having a 2.2×2.2 field of view (FOV). Wavelengths $\lambda < 2.4 \mu\text{m}$ are imaged by the short wavelength (SW) channel of each module, which has a focal plane of four abutted 2048×2048 (2040×2040 active) pixel HAWAII-2RG detectors with a plate scale of $32 \text{ mas pixel}^{-1}$. A dichroic beam splitter sends longer wavelengths to the LW channel that has a single 2048×2048 (2040×2040 active) pixel HAWAII-2RG detector focal plane with a plate scale of $65 \text{ mas pixel}^{-1}$.^{1,3} This allows simultaneous SW and LW imaging of the same NIRC*am* field with each module. The pupil wheels in the LW channels of each module are equipped with

two identical Si gratings with perpendicular orientations so that light is dispersed along either the rows (R gratings) or columns (C gratings) of their detectors. The NIRC*am* pupil wheels are located at actual pupils and are in series with filter wheels. Therefore, the gratings must be used in series with a filter wheel element. The chosen filter wheel element (filter) selects the wavelength range desired for each observation and rejects unwanted spectral orders. Each module also has two SW pupil wheel positions containing a DHS for SW spectroscopy.

This article will focus on the LW gratings as DHS performance and scientific applications have recently been described in Ref. 8. The following section describes the grism design drivers and adopted design. Their spectroscopic capabilities and expected performance in NIRC*am* are presented in the following section. That is followed by sections on planned spectroscopic operations and sample observation simulations. The paper concludes with a section on observation planning and available tools.

2 Grism Design

The grism design was driven by JWST coarse phasing wavefront sensing requirements for achieving maximum segment piston capture range and good resolution of segment piston positions (small minimum detectable piston). The gratings would be used as dispersed fringe sensors (DFSs) to measure segment piston errors.⁷ The large capture range requirement drives the design toward producing spectra at the longest possible wavelengths, and a small minimum detectable piston drives the design toward larger spectral coverage. These effects are coupled for a fixed long-wavelength cutoff: large spectral ranges provide

*Address all correspondence to: Thomas P. Greene, E-mail: tom.greene@nasa.gov

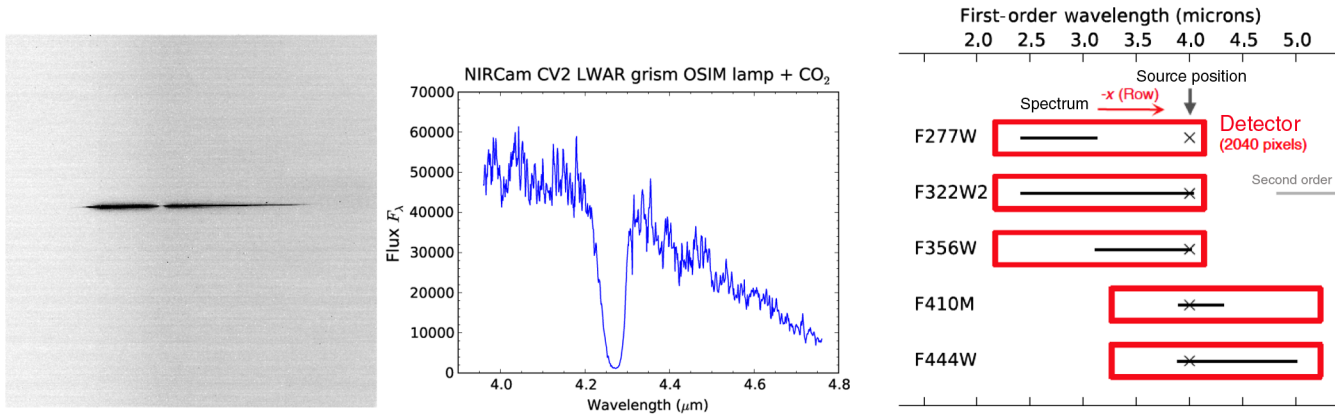


Fig. 1 (a) NIRCcam spectral image of the OSIM supercontinuum lamp taken with the LWA R grism and F444W filter during JWST instrument testing at NASA GSFC in August 2014. The image is oriented so that detector x coordinates increase to the left and wavelength increases to the right. (b) Extracted spectrum from the image with an approximate wavelength calibration applied. The continuum decreases toward longer wavelengths due to low fiber transmittance, and the broad feature near $4.27 \mu\text{m}$ is due to CO_2 absorption. Both of these features are artifacts of the test equipment and not NIRCcam itself. (c) Layout of an object's LW R grism spectra relative to its direct image position for different filters (image courtesy of D. Coe).

small minimum detectable pistons, but their relatively small SW limits reduce the maximum piston capture range. The instantaneous spectral coverage of an observation is set by spectral dispersion and is limited by finite detector size and the free spectral range of the spectral order used.

These factors drove the LW grism effective cutoff to be set to NIRCcam's LW detector and filter cutoff, $\lambda = 5.0 \mu\text{m}$. The adopted design sets spectral dispersion to be $10.0 \text{ \AA pixel}^{-1}$, producing a central undeviated wavelength $\lambda = 4.0 \mu\text{m}$ and an SW cutoff $\lambda = 3.0 \mu\text{m}$ on NIRCcam's LW detector arrays. These nominal wavelength cutoffs apply when a source is located at the center of the FOV. This large operating wavelength range dictates that the gratings operate in first order, $m = 1$.

Equation (5) of Ref. 9 shows that the maximum detectable wavefront piston error of a grism used as a DFS is $\delta L_{\text{max}} \propto R_0 \lambda_B^2$, where R_0 is the effective spectral resolving power and λ_B is the blue (SW) cutoff of the filter used with the grism. LW filters have large λ_B and therefore have large capture ranges. The effective resolving power of a grism used to phase two adjacent primary mirror segments is $R_0 = mN_0$, where N_0 is the number of grism grooves that span the distance between the

two segment centers, and $\approx 0.2 \times$ is the total number of grooves that span the pupil. Using the NIRCcam grism groove frequency 65 mm^{-1} (Table 1), the 31-mm pupil diameter,¹⁰ and $\lambda_B = 3.88 \mu\text{m}$, then the F444W filter (Table 4) gives maximum detectable piston of $\approx \pm 200 \mu\text{m}$. This physical distance is physical distance is $1/2$ of the optical δL_{max} from Eq. (5) of Ref. 9. Errors larger than this maximum piston can be detected directly from the telescope point spread function (PSF). The minimum detectable wavefront piston error is set by the smallest measurable displacement between the red and blue ends of fringes. This can be evaluated by computing the cross-dispersion centroid locations of the fringes at the LW and SW ends of a given filter bandpass. If the measurement precision of the fringe profile centroid is 0.05 pixel, then the minimum detectable piston is $\pm 0.12 \mu\text{m}$, using the F444W and F322W2 filters.^{11,12} The telescope segments are now expected to always be within the capture range of the DHS measurements, so the gratings will likely be only used for science applications and not for wavefront sensing.

Several practical issues also drove the grism design. First, the NIRCcam pupil and filter wheels are spaced closely, separated by only about 10 mm. The elements in these wheels are also large, with 48-mm diameter and 42-mm clear apertures. This requires the grism to have a small prism angle, less than about 10 deg. Given this small angle, the relatively high dispersion ($10.0 \text{ \AA pixel}^{-1}$) dictates a high refractive index, $n \lesssim 2.5$, as derived from standard first-order grism design equations.^{13,14} The grism material must also maintain high and uniform optical transmission after exposure to a significant dose of cosmic radiation over the lifetime of JWST. The radiation at JWST's L2 orbit location will be dominated by high-energy α particles, and we estimate that the total ionizing dose experienced by the gratings will be less than ~ 10 krad (Si) for a 10-year mission. This was determined from the 10-year JWST mission dose¹⁵ after adjusting for the expected 2018 launch date (near solar minimum) and the ~ 2 mm of Ti shielding the gratings. We selected monocrystalline Si as the grism material given its infrared transmission, high refractive index ($n = 3.4$ at $T = 35 \text{ K}$), and high radiation tolerance.¹⁷

The blaze angle was chosen to maximize efficiency near $\lambda = 3.7 \mu\text{m}$, the mean wavelength of the $\lambda = 2.4$ to $5.0 \mu\text{m}$

Table 1 Basic grism parameters.

Material	Optical grade monocrystalline Si
Operating temperature	~ 30 to 35 K
Groove frequency	65 mm^{-1}
Prism angle	6.16 deg
Blaze angle	5.75 deg
Maximum thickness	8.0 mm
Diameter	48.0 mm, circular with side flats
Clear aperture	42.0 mm, circular
AR coating	2.4 to $5.0 \mu\text{m}$

LW modules. This is slightly different from the undeviated wavelength ($\lambda = 4.0 \mu\text{m}$), so the blaze angle is offset slightly from the prism angle. The basic manufacturing specifications of the gratings are given in Table 1. The gratings were fabricated via microlithographic etching techniques at the University of Texas at Austin⁶ and were antireflection (AR) coated by II–VI infrared. All four flight gratings were coated on their flat faces, and two were coated on their grooved faces. Two were left uncoated on their grooved sides as a precautionary measure in case there were adhesion problems or coating nonuniformities due to the grooves. However, no such problems have been identified after several cryogenic cycles. The two gratings that were coated on both faces are located in NIRCcam module A, while the gratings that were coated only on their flat ungrooved faces are located in module B. The dispersions of all four gratings were measured to be within 1% of the $10.0 \text{ \AA pixel}^{-1}$ design value during JWST science instrument testing at NASA Goddard Space Flight Center (GSFC) during the summer of 2014.

3 Grism Spectroscopic Capabilities

3.1 Grism Usage

Filters are used in series with gratings to select the spectral bandpass desired for each observation. The NIRCcam LW filter wheel contains filters that have medium ($\lambda/\Delta\lambda \sim 8$ to 20), wide ($\lambda/\Delta\lambda \sim 4$ to 5), and extra-wide ($\lambda/\Delta\lambda \sim 1$ to 2) bandpasses, and any of these can be used with the gratings in principle.¹⁸ A subset of these is being defined for science applications. All LW narrow-band filters reside in the same pupil wheel as the gratings, so these cannot be used in series with the gratings. Each grism spans the entire pupil (image of the telescope primary), and any source in the NIRCcam imaging field will have its light dispersed by a grism that is selected in the pupil wheel. Some of the dispersed spectrum may land outside the FOV and not be recorded by the detector depending on the object field position and the selected filter (see Sec. 4). Spectra of sources slightly outside (to $\sim 10\%$ beyond the field size) of the imaging FOV can be

recorded by the detectors. The image and extracted spectrum of a NIRCcam module A LW grism exposure taken during the JWST instrument test campaign at NASA GSFC in 2014 is shown in Fig. 1. This figure also shows the layout of an object's LW R grism spectra relative to its direct image position for different filters.

The gratings are usually operated in first order ($m = 1$), where they have maximum efficiency in NIRCcam's LW bandpass. Their high dispersions, the finite size of the NIRCcam field and detectors, and the limited bandpasses of the series filters all limit the detection of other orders. It is only possible to detect $m \neq 1$ light when using the F322W2 filter with an LW grism. In that case, an object at the right location can produce a spectrum that is $m = 1$ at LWs and $m = 2$ at SW within the F322W2 bandpass (see Fig. 1 right panel).

3.2 Resolving Power, Sensitivities, and Saturation Limits

The transmittance and reflectance values of all NIRCcam optical components used for imaging observations have been measured from actual parts or test samples. The composite throughput values for module A including the optical telescope element (OTE) reflectivity as well as NIRCcam detector quantum efficiency are shown in Fig. 2. This figure also shows the theoretical first-order modules A and B LW grism efficiencies and module B grism measurements at two wavelengths and are shown as crosses. The grism efficiency must be multiplied by the NIRCcam + OTE curve for the chosen series filter to produce the total system throughput at each wavelength (not shown). Module A LW gratings are AR coated on both sides, while those in the module B are coated only on their flat (nongrooved) sides. Therefore, the module B LW grism efficiencies are ~ 0.74 times that of the module A ones, and the module B ones produce some ghosts of bright spectra.

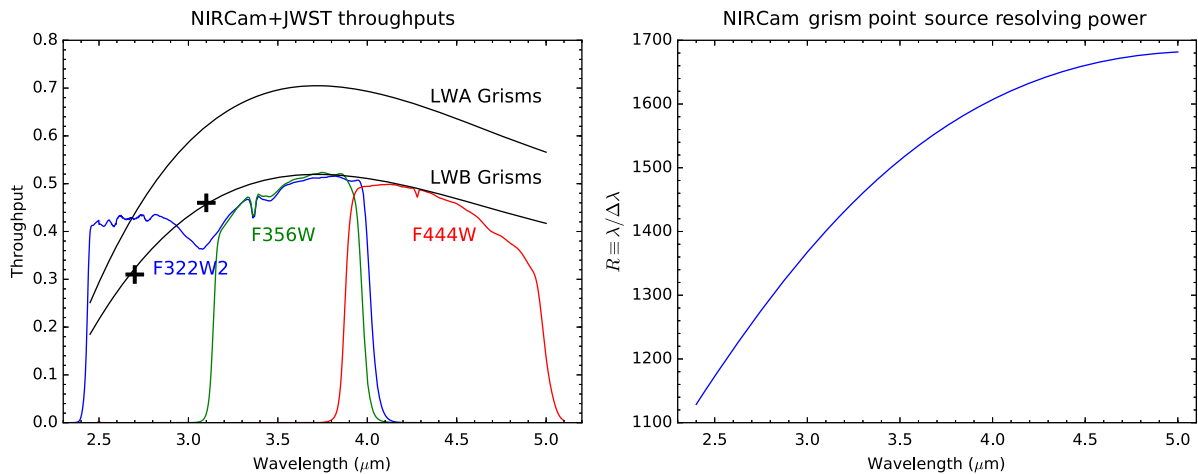


Fig. 2 (a) Total system throughput including all OTE and NIRCcam optics and the detector quantum efficiency for several NIRCcam filters (module A optics and QE shown; module B is similar). The theoretical LW grism efficiency curves must be multiplied by the optics curves for a chosen filter to produce the system throughput at each wavelength. The module B LW gratings are AR coated on only one side and therefore have throughputs $\sim 25\%$ lower than the LWA gratings. Module B grism throughputs were measured at two wavelengths and are shown as crosses. (b) Spline curve fit to the grism FWHM spectral resolving power R versus wavelength for point sources. This is limited by pixel sampling of the PSF at shorter wavelengths ($\lambda \lesssim 4 \mu\text{m}$) and by diffraction and the quasi-hexagonal pupil shape¹⁹ at longer wavelengths ($\lambda \lesssim 4 \mu\text{m}$).

All NIRCcam spectroscopy is conducted without using slits or other focal plane apertures, so the spectral resolving power R of its grism observations are determined by the dispersion, wavelength, its pupil shape,¹⁹ detector sampling, and object size. We now incorporate these into the equation for spectral resolving power, $R \equiv \lambda/\Delta\lambda$. At wavelength λ , the point-source spectral resolution is $\Delta\lambda = FWHM \times \delta\lambda$, where $FWHM$ is the full width at half maximum of the monochromatic PSF as sampled in NIRCcam LW pixels and $\delta\lambda$ is the spectroscopic dispersion, $10.0 \text{ \AA pixel}^{-1}$ (see Sec. 2). This dictates that R increases nearly linearly with the wavelength at $\lambda \lesssim 4 \mu\text{m}$, where the under-sampled PSF is ~ 2 pixels; then R increases less steeply at $\lambda \lesssim 4 \mu\text{m}$, where diffraction increases the size of the NIRCcam PSF, causing point sources to subtend more pixels. The quasi-hexagonal JWST pupil causes some light to be diffracted by fewer grism grooves than the maximum number that span the pupil ($N_{\text{max}} = 31 \text{ mm pupil}^{10} \times 65 \text{ grooves mm}^{-1}$), reducing the maximum resolving power. This effect causes a 15% increase in the spectral PSF width of a circular pupil and a corresponding reciprocal loss in resolving power.¹⁹ We estimate that the quasi-hexagonal JWST pupil causes a similar increase in the spectral PSF width over the spatial PSF, reducing the maximum resolving power to $R_{\text{max}} \approx 0.9mN_{\text{max}}$. We have incorporated this beam factor into our resolving power calculations by scaling the simulated, high-resolution monochromatic PSF by a factor of 1.1 in the spectral dimension before sampling by the NIRCcam pixels and computing the FWHM in the equation for R above. The resultant spectroscopic resolving power for LW grism observations of point sources is shown in the right panel of Fig. 2. This can also be approximated with the function

$R \approx 3.35(\lambda/\mu\text{m})^4 - 41.9(\lambda/\mu\text{m})^3 + 95.5(\lambda/\mu\text{m})^2 + 536(\lambda/\mu\text{m}) - 240$ to within a few percent. The pixel-limited resolving power (strongest at $\lambda \lesssim 4 \mu\text{m}$) may be improved with dithering of multiple observations.

Tables 2 and 3 give the 10σ point-source continuum sensitivities for the modules A and B grisms using a $2 \text{ spectral} \times 5 \text{ spatial}$ pixel extraction aperture in 10^4 s of integration time. Unresolved point-source emission line sensitivities are also given, using the spectral resolving power computed for each wavelength (right panel of Fig. 2). All sensitivities were calculated for estimated average zodiacal background levels using either the F322W2 or F444W filter in series, as identified in the table. These sensitivities are a factor of ~ 2 to 3 worse than expected for the JWST NIRSpec instrument, but NIRSpec cannot be operated in a true slitless mode.²⁰ Both NIRCcam and the NIRSpec microshutter array have similar FOV. Lower background conditions than those assumed here will give sensitivities that are up to a factor of ~ 1.4 lower (better), and higher background conditions will result in sensitivities that are up to a factor of ~ 2 higher (worse). Using narrower band filters (i.e., F356W instead of F322W2 or F410M instead of F444W) can improve sensitivities by a factor of ~ 1.2 to 2. We also show the point-source continuum and emission-line sensitivities for F322W2, F410M, and F444W filters in Fig. 3. Tables 2 and 3 also give saturation values for 0.68 s integrations, two frame times for 2048×64 pixel subarrays with the detector operated using four outputs (stripe mode). Larger subarray stripes ($2048 \times > 64$ pixels) will result in fainter bright limits, and operating in window mode (using a single detector output) will make the bright limits 1.5 mag fainter. The module B grisms

Table 2 Module A LW grism performance (F322W2 and F444W filters).

λ (μm)	F_{cont} ($\mu \text{ Jy}$) ^a	F_{line} ($\text{erg s}^{-1} \text{ cm}^{-2}$) ^b	K_{sat} (A0V) ^c	K_{sat} (M2V) ^c	Filter ^d
2.5	9.1	9.7×10^{-18}	4.3	4.2	F322W2
2.7	6.8	6.3×10^{-18}	4.4	4.4	F322W2
2.9	6.1	5.0×10^{-18}	4.3	4.3	F322W2
3.1	6.6	4.8×10^{-18}	4.1	4.1	F322W2
3.3	5.3	3.5×10^{-18}	4.1	4.3	F322W2
3.5	5.2	3.2×10^{-18}	4.0	4.2	F322W2
3.7	5.1	2.9×10^{-18}	3.9	4.1	F322W2
3.9	5.6	3.0×10^{-18}	3.7	3.9	F322W2
4.1	7.8	4.0×10^{-18}	3.4	3.7	F444W
4.3	8.7	4.3×10^{-18}	3.1	3.4	F444W
4.5	10	4.8×10^{-18}	2.9	3.0	F444W
4.7	13	5.9×10^{-18}	2.5	2.7	F444W
4.9	17	7.5×10^{-18}	2.1	2.4	F444W

^a 10σ point-source continuum sensitivities for 10,000 s integrations using a $2 \text{ (spectral)} \times 5 \text{ (spatial)}$ pixel extraction aperture.

^b 10σ point-source unresolved emission line sensitivities for 10,000 s integrations using the actual FWHM PSF size and consequent spectral resolving power at this wavelength (right panel of Fig. 2).

^cK-band vega magnitudes for saturation (80% full well or 65,000 electrons) for 0.68 s integrations (two reads) of 2048×64 pixel regions in stripe mode (four outputs). Larger subarrays or use of only one output will result in fainter bright limits.

^dNarrower filters will have similar saturation values and somewhat smaller (better) sensitivities.

Table 3 Module B LW grism performance (F322W2 and F444W filters).

λ (μm)	F^{cont} (μJy) ^a	F_{line} ($\text{ergs}^{-1} \text{cm}^{-2}$) ^b	K_{sat} (A0V) ^c	K_{sat} (M2V) ^c	Filter ^d
2.5	11	1.2×10^{-17}	3.8	3.8	F322W2
2.7	8.6	7.9×10^{-18}	4.0	3.9	F322W2
2.9	7.7	6.2×10^{-18}	3.9	3.9	F322W2
3.1	8.2	5.9×10^{-18}	3.7	3.7	F322W2
3.3	6.5	4.3×10^{-18}	3.8	3.9	F322W2
3.5	6.2	3.8×10^{-18}	3.6	3.9	F322W2
3.7	6.0	3.4×10^{-18}	3.6	3.8	F322W2
3.9	6.3	3.3×10^{-18}	3.4	3.6	F322W2
4.1	9.5	4.8×10^{-18}	3.1	3.4	F444W
4.3	10	5.0×10^{-18}	2.9	3.2	F444W
4.5	12	5.4×10^{-18}	2.7	2.8	F444W
4.7	14	6.3×10^{-18}	2.3	2.6	F444W
4.9	17	7.4×10^{-18}	2.0	2.3	F444W

^a 10σ point-source continuum sensitivities for 10,000 s integrations using a 2 (spectral) \times 5 (spatial) pixel extraction aperture.

^b 10σ point-source unresolved emission line sensitivities for 10,000 s integrations using the actual FWHM PSF size and consequent spectral resolving power at this wavelength (right panel of Fig. 2).

^cK-band vega magnitudes for saturation (80% full well or 65,000 electrons) for 0.68 s integrations (two reads) of 2048×64 pixel regions in stripe mode (four outputs). Larger subarrays or use of only one output will result in fainter bright limits.

^dNarrower filters will have similar saturation values and somewhat smaller (better) sensitivities.

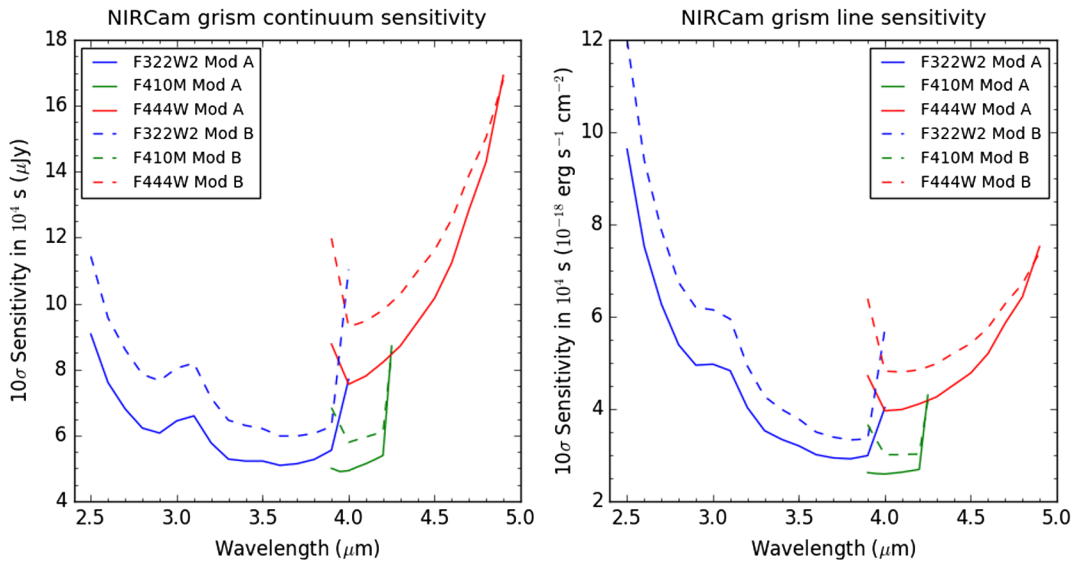


Fig. 3 (a) Point-source continuum and (b) emission line sensitivities are shown for grisms with F322W2, F410M, and F444W filters for both modules A and B. Note that the narrower bandwidth of the F410 filters results in significantly better sensitivity than the wider F444W at common wavelengths.

(Table 3) provide slightly larger (worse) sensitivities and brighter saturation limits than the module A ones (Table 2) because the module B grisms are AR coated on only one side, and there are slight differences in the optical transmissions and detector quantum efficiencies between the modules.

4 Spectroscopic Operations

The NIRCcam LW grisms are expected to be used in either of two modes: single-object time-series slitless spectroscopy or wide-field (multiobject) slitless spectroscopy. The layout of the grism dispersions on the NIRCcam LW detectors and in the JWST focal

plane is shown in Fig. 4. A single object can be positioned at the appropriate point to have its entire spectrum (as limited by the chosen filter) fall onto the detector array. Spectra of multiple objects in the imaging field will be recorded, and large sky areas can be mapped with multiple telescope pointings. The gratings can be operated in series with any filter in the NIRCcam LW pupil wheel in principle, and the numerous choices allow optimization for spectral coverage, confusion, or sensitivity. Table 4 lists all the wide- and some of the medium-band filters that will be enabled for use with the gratings during JWST observing cycle 1. We expect those to be most popular, and the remaining medium-band LW filters (F250M, F300M, F335M, F360M, F410M, and F480M) will also be available for use in wide-field mode in cycle 1 and later.

The relatively high dispersion of the gratings cause spectra at extreme wavelengths (i.e., $\lambda < 3 \mu\text{m}$ and $\lambda \sim 5 \mu\text{m}$) to be displaced significantly (~ 1024 pixels or more) from the image location of the observed object in the dispersion direction. This means that wide-field grism observations taken with filters operating at extreme wavelengths will observe objects in an area considerably smaller than the full imaging field. For example, spectra taken with the F277W filter will fill only about half of

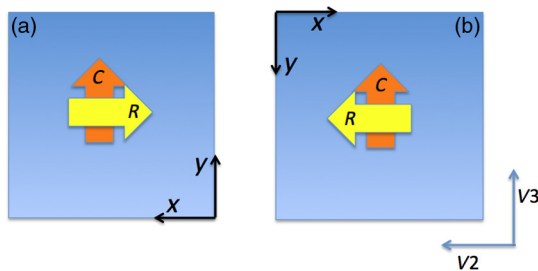


Fig. 4 Grism dispersion orientations along detector axes (x, y) and the JWST observatory axes ($V2, V3$). The $V3$ position angle is defined to be 0 deg when $V2$ points east and $V3$ points north in the sky. The yellow and orange arrows point in the direction of increasing wavelength for R and C gratings in (a) module A and (b) module B, respectively. Each module has a 2.2×2.2 imaging FOV.

Table 4 Popular filters available for use with LW gratings.

Filter name ^a	λ_1 (μm) ^b	λ_2 (μm) ^c	# dispersed pixels	# pixels/2040 ^d	Mode ^e
F277W	2.416	3.127	711	0.35	TS + WF
F322W2	2.430	4.013	1583	0.77	TS + WF
F356W	3.140	3.980	840	0.41	TS + WF
F444W	3.880	4.986	1106	0.54	TS + WF
F430M	4.167	4.398	231	0.11	WF
F460M	4.515	4.747	232	0.11	WF

^aAll LW M filters will also be available in wide-field mode; F430M and F460M are expected to be popular and are included for illustrative purposes.

^bHalf-power wavelength (blue side).

^cHalf-power wavelength (red side).

^dFraction of the detector that a continuum spectrum occupies in the dispersion direction.

^eTS, single-object time series; WF, wide-field modes.

the detector area. The missing spectra in the unfilled area would have object images outside the NIRCcam imaging FOV (see also Sec. 3.1). Objects further than $\sim 10\%$ outside the imaging field do not illuminate the NIRCcam pick-off mirror and therefore cannot be observed.

The NIRCcam detectors will be operated in their normal MULTIACCUM modes^{21–23} during spectroscopic observations. High-precision time-series grism observations of bright objects (e.g., host stars of transiting planets) will likely require the use of a limited detector region to prevent saturation. Subarrays consisting of 64, 128, 256, or the full 2048 (including reference pixel) detector rows will be supported for single-object time-series LW grism observations. These can be read out either using all four outputs (stripe mode, spanning all 2048 columns) or in window mode using a single output and possibly a smaller number of columns. Using the combination of stripe mode and 64 detector rows gives the fastest readout time and provides the best bright limits (see Sec. 3.2, Tables 2 and 3).

LW grism spectral observations can be partnered with simultaneous imaging observations of the same field in the SW channels. SW imaging observations can be conducted infocus using only filters (in both LW spectroscopic modes) or out of focus using a weak lens with a filter in series (single-object time-series mode only). Given the flux differences between dispersed spectra and infocus images, we expect that many single-object point-source observers will opt for using a weak lens in series with the LW gratings. It may be possible to obtain SW $\lambda = 1$ to $2 \mu\text{m}$ DHS spectra simultaneously with LW grism spectra if and when the DHSs are supported for scientific use.⁸

All NIRCcam detectors will be operated with the same readout pattern and subarray size, so SW observations will use the same size detector region (full frame or subarray) as used for the LW gratings. At least 96% of the light from a point source using weak lens WLP8 (eight waves of defocus at $2.12 \mu\text{m}$) in the SW channel will fall within a 2048×128 pixel subarray aperture. Although the SW and LW subarrays have the same dimensions, their locations on the detectors can be individually specified. Tailoring of the SW and LW subarray positions is necessary because the SW pixel scale ($32 \text{ mas pixel}^{-1}$; see Sec. 1) is approximately half that of the LW channel. This causes the image of an object to fall at substantially different detector positions on the SW and LW detectors. The SW image can appear on different SW detectors, depending on where the source is in the LW field. When SW imaging or DHS data are taken in parallel with the LW grism data, particular care must be exercised to ensure that the single set of exposure parameters provides adequate dynamic range in both the SW and LW channels.

Most single-object time-series integrations will likely use the RAPID (every frame sample saved) or BRIGHT1 (every other frame sample saved) MULTIACCUM detector operation modes. This will produce a large amount of data, especially when conducting simultaneous SW and LW grism observations as they will use two (LW grism + SW imaging) or three detector arrays (LW grism + DHS if DHS use is implemented). The on-board solid-state data recorder (SSR) can store 7 to 10 h of RAPID data for three detector arrays operated in stripe mode (four outputs) and 28 to 40 h of data when the detectors are operated with single outputs. JWST is expected to download data every 12 h, so all but the longest transits of the brightest stars can be observed with both an LW grism and an SW element without overflowing the SSR.

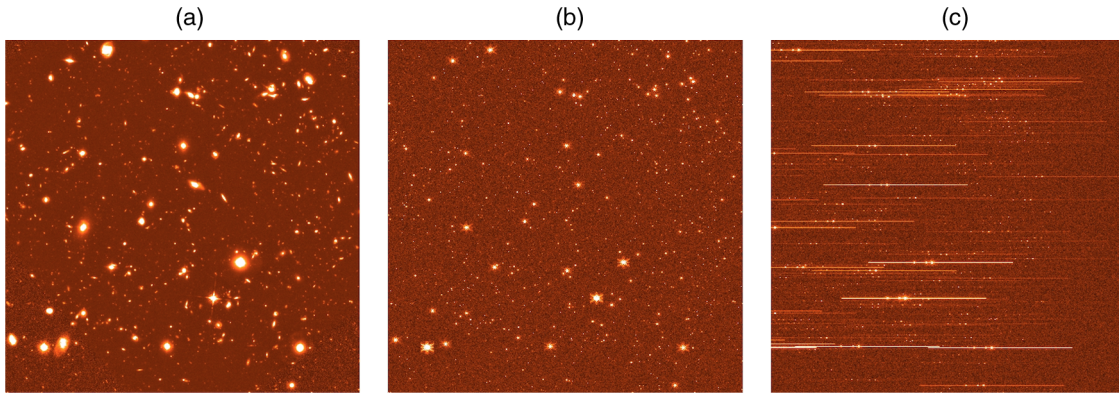


Fig. 5 (a) HST/WFC3-IR F160W image of the Hubble XDF³⁰ covering the area around the Hubble ultra-deep field. The total exposure time is ~ 65 h over most of the image; (b) 2-h JWST NIRCcam image in the F356W filter simulated with the source catalog produced from the XDF F160W image on the left. For simplicity, all the sources were assumed to be point-like (i.e., represented by the simulated WebbPSF F356W PSF) and $m_{356,AB} = m_{160,AB}$; (c) simulated 2-h NIRCcam module A R grism data with the F356W filter. The input model spectrum was constructed as a combination of a flat F_ν flux continuum and three emission lines, $H\beta$ and [O III] 4959/5007 Å lines, with rest-frame equivalent widths of ~ 180 , 200, and 600 Å, respectively (the line widths are unresolved). All sources were redshifted to $z = 6$ to illustrate the detectability of the three emission lines as a function of source brightness. The images are oriented with north up and east to the left, and wavelength increases to the right (as in Fig. 4 with V3 PA = 0 deg.)

5 Simulations of Spectroscopic Observations

We have developed software tools to simulate NIRCcam spectroscopic LW grism observations to assess expected performance and to plan using NIRCcam in both single-object and multiobject wide-field slitless spectroscopy modes. We describe these tools and present some results in this section.

The first simulator is designed to produce spectral images from multiple objects distributed in two spatial dimensions within a given NIRCcam field. We have implemented this using the aXeSIM package, first developed for simulating HST WFC3 slitless spectroscopic images.²⁴ Spectra of individual objects can be extracted from simulated images using the companion aXe package²⁵ or other conventional astronomical data tools. We have produced aXeSIM configuration files that produce the expected signal and noise performance of the NIRCcam LW grisms as we expect them to be used on JWST. In addition to producing the wide-field slitless spectroscopy simulations in this section, we have used aXeSIM to validate the NIRCcam performance estimates given in Table 2. aXeSIM-derived estimates agree within $\sim 10\%$ of pyNRC, the internal NIRCcam team exposure time calculator (ETC).²⁶ The corresponding author of this publication will provide a package of the NIRCcam LWA R grism configuration files for use with aXeSIM upon request. The recently released JWST ETC can also be used to simulate and plan wide-field slitless spectroscopy observations (see Sec. 6).²⁷

We have also developed a second simulator that is used to estimate the signals and noise expected for high precision time-series observations of transiting planet spectra. These codes include the same throughputs (e.g., Fig. 2) used in the aXeSIM configuration files, and they also include an expected systematic noise floor in addition to the regular noise terms for detector read noise, dark noise, and observatory background noise components. One-dimensional simulations of exoplanet transmission (in transit) or emission (in secondary eclipse) spectra are produced, and they are described further in Ref. 28. The PandExo²⁹ transiting exoplanet tool can also be used to simulate

and plan spectroscopic observations of transiting planets (see Sec. 6).

5.1 Wide-Field Slitless Spectroscopy of Extragalactic Fields

JWST is expected to revolutionize the study of high-redshift galaxies, allowing spectroscopic study of familiar rest-frame optical emission lines at high redshifts. With a wavelength coverage of 2.4 to $5 \mu\text{m}$, the NIRCcam LW grism mode can detect $H\alpha$ at $z = 2.7$ to 6.6, [O III] 5007 Å at $z = 3.8$ to 9.0, and [O II] 3727 Å at $z = 5.4$ to 12.4. Although NIRSspec will be the preferred choice for most extragalactic spectroscopic observations because of its superior sensitivity and wider wavelength coverage (1 to $5 \mu\text{m}$ for $R = 1000/2700$ and 0.7 to $5.0 \mu\text{m}$ for $R = 100$), the NIRCcam LW grism mode does offer some interesting and potentially powerful capabilities. For example, the NIRCcam LW grism mode will allow: (1) blind searches for strong line emitters at high redshift; (2) spatially resolved spectroscopy for a large number of galaxies simultaneously; and (3) spectroscopic surveys without preimaging data (well suited for parallel programs).

Figure 5 shows the aXeSIM simulation of a 2-h NIRCcam LW grism exposure taken over the extreme deep field³⁰ (XDF) using the F356W filter. Here, the redshifts of all the sources have been set to 6 artificially to illustrate the detectability of $H\beta$ and [O III] 4959/5007 Å lines as a function of source brightness. In this image, the continuum is visible down to ~ 24 AB mag ($\sim 1 \mu\text{Jy}$), while emission lines are visible down to $\sim 2 \times 10^{-18}$ erg cm^{-2} s^{-1} . Although the confirmation of actual sensitivities has to wait for inorbit observations, this simulation clearly demonstrates that NIRCcam LW grism observations of extragalactic fields will produce rich data sets.

Recent studies indicate that the rest-frame optical emission lines of some $z \sim 7$ galaxies are quite luminous and have large equivalent widths.³¹ The combined rest-frame equivalent width of $H\beta$ + [O III] 4959/5007 Å lines can be well over 1000 Å and could reach as high as 2000 to 3000 Å in some cases (e.g., Smit

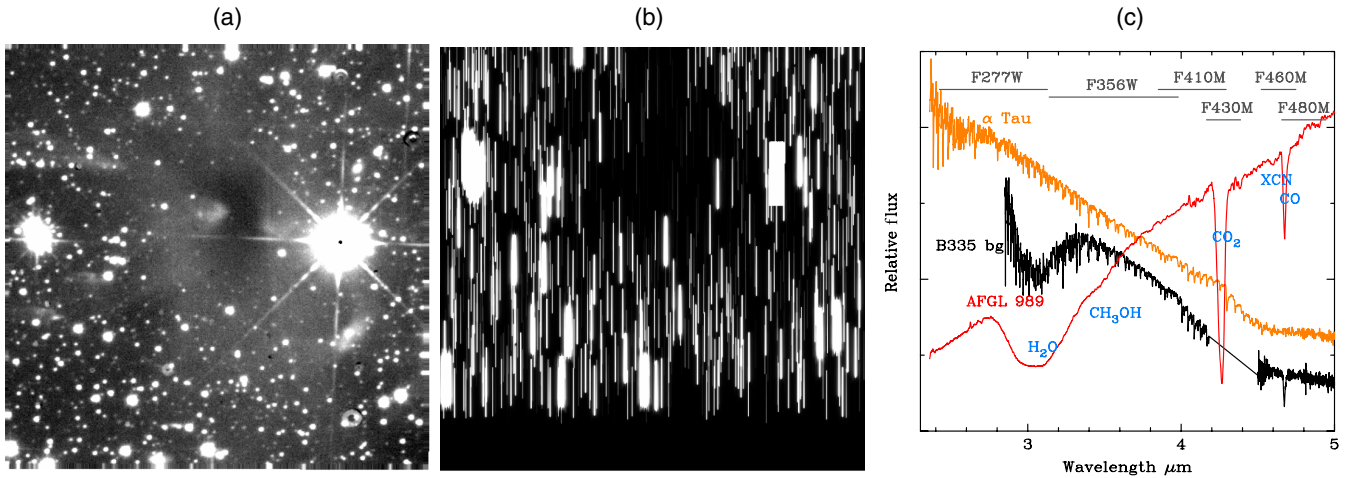


Fig. 6 (a) B335 dark cloud K -band ($\lambda = 2.2 \mu\text{m}$) UKIRT image acquired in 3.2 h integration time. (b) Simulated 0.45 h JWST NIRCcam spectral image using the module A C grism and F430M filter, using simulated PSFs for $K = 20$ mag (vega) and brighter stars in the UKIRT data, and fainter stars added using the TRILEGAL background model³⁵ with measured extinctions applied. Spectra are vertically offset from the UKIRT image because the $\lambda = 4.0 \mu\text{m}$ undeviated wavelength is outside the bandpass of the F430M filter. (c) Interstellar ice spectra are shown with NIRCcam filter bandpasses. A star behind the B335 cloud (black) is the same spectral type as α Tau³⁶ (orange), but it shows $\lambda = 3 \mu\text{m}$ H_2O and CO ice absorption due to the intervening B335 cloud. The infrared space observatory spectrum of AFGL 989³⁷ shows numerous strong and weak ice features that NIRCcam will detect and measure, including $\lambda = 4.3 \mu\text{m}$ CO_2 absorptions from ice mantles forming on dust grains in the cloud.

et al.³¹). This suggests that, although the NIRCcam LW grism mode is not as sensitive as NIRSpec, it may be quite effective at finding high-redshift galaxies through a blind search for strong line emitters (note the high signal-to-noise emission lines in Fig. 5).

5.2 Wide-Field Slitless Spectroscopy of Dark Clouds

Sun-like stars form in nearby dark clouds within our galaxy; the gas and dust within these regions are pulled together by gravity until the central regions form stars. These gravitationally-confined dark globules are very dense and emit no visible light, but they can be studied using the infrared light of background stars.^{32,33} The amount of dust (silicate and carbon grains) and gas material in these clumps can be measured by observing the brightness of these background stars at several different infrared wavelengths using NIRCcam filter imaging.

These dark molecular clouds shield the dust particles inside them from high-energy ultraviolet radiation of the interstellar radiation field. Under these shielded conditions, the gas in the clouds can freeze on dust grains and form mantles of ice. These ice mantles bring thousands of atoms and molecules into close proximity and are therefore the site of chemical reactions that begin to form more complex molecules, such as H_2O , CO , CO_2 , and H_3COH . Complex organic molecules can then form from these simple ones.³⁴

The amount of H_2O , CO , CO_2 , and perhaps other ice on a cloud's dust grains can be measured with NIRCcam LW grism spectra, as simulated using aXeSIM for the B335 cloud in Fig. 6. Background stars in high extinction regions of B335 show little overlap in their relatively short spectra through F430M (CO_2) or F460M (CO) filters, and most overlaps can be resolved with additional observations taken with the grism having dispersion in the perpendicular direction. Observations like these will show how the density of star-forming clouds changes with location and

how volatile materials freeze onto dust grains in the dense parts of clouds that may eventually form stars and planetary systems.

5.3 Spectra of Transiting Planets

We have used our one-dimensional spectral time-series simulator to model the expected JWST spectra of several transiting

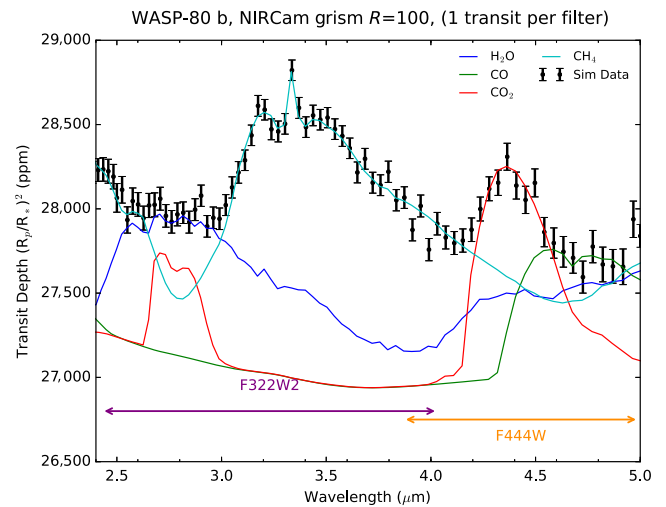


Fig. 7 Simulated transmission spectrum (black points with error bars) for the gas giant planet WASP-80 b³⁸ when observing with a NIRCcam LWA grism paired with the F322W2 filter for one transit and with the F444W filter for one other transit, binned to $R = 100$. We model the planet's spectrum with CHIMERA^{39,40} assuming a uniform temperature of 810 K, 7.5 times solar metallicity, and molecular mixing ratios consistent with chemical equilibrium. The figure shows the contributions of H_2O (water), CO (carbon monoxide), CO_2 (carbon dioxide), and CH_4 (methane) to the spectrum. The NIRCcam grism modes are especially sensitive to the carbon-bearing molecules. The wavelength coverages of each individual transit for the F322W2 and F444W filters are also shown near the bottom of the plot.

planets and estimate their scientific information content.²⁸ The simulated LW grism transmission spectra of WASP-80 b³⁸ is shown in Fig. 7. The spectral contributions of its major atmospheric constituents were modeled with CHIMERA^{39,40} and are shown as solid colored curves, with the composite model spectrum being the highest value (largest absorption) at each wavelength. We binned the simulated observations of this model planet to spectroscopic resolving power $R = 100$ and show these points as black data points with error bars indicating their uncertainties. These observations would have to be made during two separate transits: one transit with a grism plus the F322W2 filter and one with a grism and the F444W filter. SW observations can be made simultaneously with the LW grism exposures (see Sec. 4). This figure shows that NIRCam grism spectra are sensitive to strong CO (carbon monoxide) and CO₂ (carbon dioxide) features in hot planets $T > 1000$ K as well as CH₄ (methane), which is seen in cool planets, $T \leq 1000$ K and water (H₂O), which is ubiquitous in many planets. When combined with data at shorter wavelengths, these observations should constrain the metallicities, H₂O, CH₄, and CO mixing fractions of similar transiting planets to a factors of ~ 5 , much better than any current observations or shorter wavelength JWST data alone.²⁸

6 Observation Planning

The information provided above should be sufficient for assessing the basic feasibility of most NIRCam slitless spectroscopic observations. The Space Telescope Science Institute, the JWST science operations center, has developed detailed planning tools for determining integration times and designing observation sequences.

The new (as of 2017) JWST ETC tool²⁷ incorporates all NIRCam modes supported for cycle 1 observations, including wide-field and time-series spectroscopy with the LW grisms. The user generates a scene of sources and specifies observing parameters, and then ETC calculates signal-to-noise and other parameters. As described in Sec. 5, we can also provide NIRCam-specific configuration files for the aXeSIM package that can be used to simulate NIRCam LW grism observations and estimate their signal-to-noise. The PandExo²⁹ tool uses the Pandeia engine of the JWST ETC to create observation simulations of all supported JWST time-series spectroscopy modes, including the NIRCam LW grisms. Once the needed integration time has been calculated (e.g., from the ETC, aXeSIM, PandExo, or Tables 2 and 3), observation details can be planned with the Astronomer's Proposal Tool (APT) for JWST.⁴¹ Current (version 25.0.5) and later versions of APT include templates for LW grism wide-field and single-object time-series observing modes. These templates allow selection of targets, detector readout (and subarray) parameters, filters, grisms, and (for the wide-field mode) mosaics and dithers. APT provides estimates of observing visibility windows for targets (consistent with the nominal launch date, orbit, and field of regard restrictions), as well as observing overheads.

Acknowledgments

We thank D. Jaffe and his group at the University of Texas at Austin for fabricating and delivering the NIRCam grisms with excellent performance. Two anonymous reviewers provided comments that helped improve this contribution significantly. We also thank D. Coe for preparing the figure showing the layout of grism spectra in Fig. 1 and S. Lilly for discussions and

assistance with determining the LW grism dispersion orientations. We also thank N. Lewis for operations information and M. Robberto for comments on spectral resolving power. TPG and coauthors acknowledge funding support by the NASA JWST project for NIRCam, NASA WBS 411672.05.05.02.02. The authors have no relevant financial interests in the paper and no other potential conflicts of interest.

References

1. C. A. Beichman et al., "Science opportunities with the near-IR camera (NIRCam) on the James Webb Space Telescope (JWST)," *Proc. SPIE* **8442**, 84422N (2012).
2. J. E. Krist et al., "Hunting planets and observing disks with the JWST NIRCam coronagraph," *Proc. SPIE* **6693**, 66930H (2007).
3. M. J. Rieke, D. Kelly, and S. Horner, "Overview of James Webb Space Telescope and NIRCam's role," *Proc. SPIE* **5904**, 590401 (2005).
4. T. Greene et al., "Observing exoplanets with the JWST NIRCam grisms," *Proc. SPIE* **6693**, 66930G (2007).
5. T. P. Greene et al., "Slitless spectroscopy with the James Webb Space Telescope near-infrared camera (JWST NIRCam)," *Proc. SPIE* **9904**, 99040E (2016).
6. D. T. Jaffe et al., "Fabrication and test of silicon grisms for JWST-NIRCam," *Proc. SPIE* **7010**, 70103L (2008).
7. F. Shi et al., "NIRCam long wavelength channel grisms as the dispersed fringe sensor for JWST segment mirror coarse phasing," *Proc. SPIE* **7010**, 70102E (2008).
8. E. Schlawin et al., "Two NIRCam channels are better than one: how JWST can do more science with NIRCam's short-wavelength dispersed Hartmann sensor," *Publ. Astron. Soc. Pac.* **129**, 015001 (2017).
9. F. Shi et al., "Segmented mirror coarse phasing with a dispersed fringe sensor: experiments on NGST's wavefront control testbed," *Proc. SPIE* **4850**, 318 (2003).
10. L. W. Huff, "NIRCam instrument optics," *Proc. SPIE* **5904**, 590404 (2005).
11. F. Shi, "Determine the DFS minimum detectable piston by measuring fringe tilt".
12. F. Shi, "Preliminary design of JWST's backup DFS in NIRCam long wavelength channel October 26 update".
13. D. J. Schroeder, *Astronomical Optics*, 2nd ed., Academic Press, San Diego (2000).
14. J. T. Rayner, "Evaluation of a solid KRS-5 grism for infrared astronomy," *Proc. SPIE* **3354**, 289 (1998).
15. J. L. Barth, J. C. Isaacs, and C. Poivey, "The radiation environment for the next generation space telescope," 2000, https://bhi.gsfc.nasa.gov/documents/Mission_Concept_Work/ISAL_January_2002_SST/ISAL-1/Super_Star_Tracker/ngst_rad_env2.pdf (19 May 2017).
16. B. J. Frey, D. B. Leviton, and T. J. Madison, "Temperature-dependent refractive index of silicon and germanium," *Proc. SPIE* **6273**, 62732J (2006).
17. J. Schubert et al., "Alpha-radiation tests on the transmission of cryogenically cooled infrared filter materials used in ISOPHOT," *Proc. SPIE* **2553**, 288 (1995).
18. J. L. Barth, "NIRCam filters," 2002, https://bhi.gsfc.nasa.gov/documents/Mission_Concept_Work/ISAL_January_2002_SST/ISAL-1/Super_Star_Tracker/ngst_rad_env2.pdf (19 May 2017).
19. E. F. Erickson and D. Rabanus, "Beam shape effects on grating spectrometer resolution," *Appl. Opt.* **39**, 4486–4489 (2000).
20. Space Telescope Science Institute, "NIRSpec overview," 2017, <https://jwst-docs.stsci.edu/display/JTI/NIRSpec+Overview> (19 May 2017).
21. B. J. Rauscher et al., "Detectors for the James Webb space telescope near-infrared spectrograph. I. Readout mode, noise model, and calibration considerations," *Publ. Astron. Soc. Pac.* **119**, 768–786 (2007).
22. C. Beichman et al., "Observations of transiting exoplanets with the James Webb Space Telescope (JWST)," *Publ. Astron. Soc. Pac.* **126**, 1134–1173 (2014).
23. Space Telescope Science Institute, "NIRCam detector readout patterns," 2017, <https://jwst-docs.stsci.edu/display/JTI/NIRCam+Detector+Readout+Patterns> (19 May 2017).
24. Space Telescope Science Institute, "The slitless simulation package aXeSIM," 2010, <http://axe.stsci.edu/axesim/> (19 May 2017).

25. M. Kümmel et al., “The slitless spectroscopy data extraction software aXe,” *Publ. Astron. Soc. Pac.* **121**, 59–72 (2009).
26. J. Leisenring, “pyNRC—a JWST NIRCcam ETC,” 2017, <https://github.com/JarronL/pynrc> (19 May 2017).
27. Space Telescope Science Institute, “Welcome to the JWST exposure time calculator,” 2017, <https://jwst.etc.stsci.edu/> (19 May 2017).
28. T. P. Greene et al., “Characterizing transiting exoplanet atmospheres with JWST,” *Astrophys. J.* **817**, 17 (2016).
29. N. E. Batalha et al., “PandExo: a community tool for transiting exoplanet science with JWST & HST,” *Publ. Astron. Soc. Pac.* **129**, 064501 (2017).
30. G. D. Illingworth et al., “The HST eXtreme deep field (XDF): combining all ACS and WFC3/IR data on the HUDF region into the deepest field ever,” *Astrophys. J. Suppl. Ser.* **209**, 6 (2013).
31. R. Smit et al., “Evidence for ubiquitous high-equivalent-width nebular emission in $z \sim 7$ galaxies: toward a clean measurement of the specific star-formation rate using a sample of bright, magnified galaxies,” *Astrophys. J.* **784**, 58 (2014).
32. C. J. Lada et al., “Dust extinction and molecular gas in the dark cloud IC 5146,” *Astrophys. J.* **429**, 694–709 (1994).
33. C. J. Lada, J. F. Alves, and M. Lombardi, “Near-infrared extinction and molecular cloud structure,” in *Protostars and Planets V*, pp. 3–15, University of Arizona Press, Tucson (2007).
34. A. C. A. Boogert, P. A. Gerakines, and D. C. B. Whittet, “Observations of the icy universe,” *Annu. Rev. Astron. Astrophys.* **53**, 541–581 (2015).
35. L. Girardi et al., “Star counts in the galaxy. Simulating from very deep to very shallow photometric surveys with the TRILEGAL code,” *Astron. Astrophys.* **436**, 895–915 (2005).
36. L. Decin et al., “ISO-SWS calibration and the accurate modelling of cool-star atmospheres. I. Method,” *Astron. Astrophys.* **364**, 137–156 (2000).
37. E. L. Gibb et al., “Interstellar ice: the infrared space observatory legacy,” *Astrophys. J. Suppl. Ser.* **151**, 35–73 (2004).
38. A. H. M. J. Triaud et al., “WASP-80b: a gas giant transiting a cool dwarf,” *Astron. Astrophys.* **551**, A80 (2013).
39. M. R. Line et al., “A systematic retrieval analysis of secondary eclipse spectra. I. A comparison of atmospheric retrieval techniques,” *Astrophys. J.* **775**, 137 (2013).
40. M. R. Line et al., “A systematic retrieval analysis of secondary eclipse spectra. II. A uniform analysis of nine planets and their C to O ratios,” *Astrophys. J.* **783**, 70 (2014).
41. Space Telescope Science Institute, “Astronomer’s proposal tool,” 2017, <http://www.stsci.edu/hst/proposing/apt> (19 May 2017).

Thomas P. Greene received his PhD in astronomy from the University of Arizona in 1991 and held positions at the University of Hawaii Institute for Astronomy and the Lockheed Martin Advanced Technology Center before joining Ames in 1998. He is an astrophysicist at NASA’s Ames Research Center in Mountain View, California. He is a coinvestigator on the JWST NIRCcam instrument and a member of the JWST midinfrared science team; he studies young stars and extrasolar planets.

Biographies for the other authors are not available.